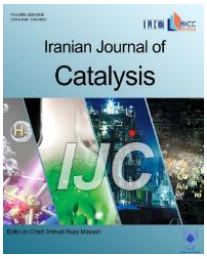

Iran. J. Catal. 2026; 16(1): 19-37

Iranian Journal of Catalysis (IJC)

https://doi.org/10.57647/ijc.2026.1601.02

Research Article

Synthesis of Iron and Nickel- Based Catalysts for Levulinic Acid Production from Cellulose and Glucose

Zulkipli Nor Akhlisah[1,2,*], W.A.K.G Wan Azlina[1,*], Robiah Yunus[1], Yun Hin Taufiq-Yap[3], Umer Rashid[4,5,6], G. Abdulkareem-Alsultan[2], N. Asikin-Mijan[7]

[1]*Sustainable Process Engineering Research Centre (SPERC), Department of Chemical & Environmental Engineering, Faculty of Engineering, University Putra Malaysia, 43400 UPM Serdang, Selangor, Malaysia*

[2]*School of Engineering, Faculty of Engineering and Technology, Sunway University, Jalan Universiti, Bandar Sunway, Selangor, 47500, Malaysia*

[3] *Center of Excellence for Catalysis Sciences and Technology, Faculty of Sciences, University Putra Malaysia, UPM Serdang, Selangor, Malaysia*

[4] *Faculty of Applied Sciences, UCSI University, No 1, Jalan UCSI, UCSI Heights, 56000 Cheras, Kuala Lumpur, Malaysia*

[5] *Department of Chemical Technology, Faculty of Science, Chulalongkorn University, Pathumwan, Bangkok 10330, Thailand*

[6] *Center of Excellence in Catalysis for Bioenergy and Renewable Chemicals (CBRC), Facualty of Science, Chulalongkorn University, Pathumwan, Bangkok 10330, Thailand*

[7]*Department of Chemical Sciences, Faculty of Science and Technology, University Kebangsaan Malaysia, UKM Bangi, Selangor, Malaysia*

[*] **Corresponding authors:** wanazlina@upm.edu.my, akhlisahzn@gmail.com

Article History:

Received:
27 March 2025

Revised:
30 September 2025

Accepted:
04 November 2025

Published Online:
25 November 2025

Published in Issue:
31 March 2026

Abstract

The study explores the catalytic performance of nickel (Ni) and iron (Fe)-based catalysts synthesized through precipitation, activation by hydrothermal reaction, and calcination for the conversion of cellulose and glucose into levulinic acid (LA). Characterization of the catalysts was conducted using X-ray diffraction (XRD) and Fourier-transform infrared spectroscopy (FTIR) analyses, which confirmed the formation of metal oxides, specifically NiO and Fe_2O_3, in the synthesized catalysts. The key experimental parameters, including catalyst loading, reaction temperature, and time, were optimized to improve the LA yield. The Fe.75Ni catalyst achieved the highest catalytic activity, yielding 46.18% based on the theoretical yield or a weight percentage of 29.72 wt.% at a reaction time of 5 hours and 200°C reaction temperature using 0.30g of catalyst. The study highlights the importance of catalyst acidity, good surface area, and thermal stability in enhancing LA production and suggests that the Fe.75Ni catalyst holds significant potential for efficient conversion of biomass.

Keywords: Conversion; Characterization; Heterogeneous catalyst; Levulinic acid; Metal oxide

Cite this article: Z. N. Akhlisah, W.A.K.G Wan Azlina, R. Yunus, Y. Hin Taufiq-Yap, U. Rashid, G. Abdulkareem-Alsultan, N. Asikin-Mijan, Iran. J. Catal. **16** (2026) 19-37. https://doi.org/10.57647/ijc.2026.1601.02

1. Introduction

Typically, the conversion of biomass involves dehydration of cellulose, resulting in the production of many platform chemicals such as levulinic acid (LA) and 5-hydroxymethylfurfural (HMF) [1]. As a short-chain fatty acid, LA contains both an acidic carboxyl group and a ketone carbonyl group, enabling it to be a feedstock for

a wide range of chemical compounds [2]. Lignocellulosic biomasses with high cellulose content are currently the most studied and widely available raw materials for LA synthesis [3]. Despite its potential, there are significant challenges that need to be addressed in the conversion of biomass. The primary difficulty lies in the resistance of lignocellulose to being broken down, particularly the cellulose [4]. The hemicellulose and cellulose within the biomass are intricately linked and bound to lignin, creating a robust structure that is difficult to process [5]. Nevertheless, utilization of cellulose as well as glucose as the starting materials to produce LA has shown considerable promise, given that both materials can be converted into HMF, before being rehydrated into LA [6]. Typical methods to produce LA from lignocellulose are using homogeneous and non-recyclable catalysts. A significant challenge in the conversion of biomass is the disposal of this catalyst, which is commonly discarded in sewage systems, further exacerbating environmental issues [7]. To address this problem, researchers are increasingly exploring the use of heterogeneous catalysts in the biomass conversion process. Heterogeneous catalysts offer several advantages over homogeneous catalysts. They can easily separate and recover from the reaction medium without requiring a neutralizing chemical [8]. The ability of heterogeneous catalysts to enable catalytic processes that are both reusable and more environmentally friendly has made them a focus of extensive research in the field of biomass conversion. This approach holds significant promise for developing efficient and sustainable methods for the conversion of lignocellulosic biomass into valuable chemicals and fuels. Metal salts such as metal oxides, metal chlorides, and metal triflates are commonly used heterogeneous catalysts, better known as Lewis acid catalysts, in the conversion of biomass. It is well-established that metal oxide species are formed during the hydrolysis of metal halides, such as metal chlorides, in the presence of water at high temperatures. This hydrolysis process leads to the formation of hydroxide (OH) ligands, which act as electron pair donors, and the presence of these OH ligands enhances the acidity of the metal cations by enhancing their electron-accepting capability [9]. The metal chlorides, namely $FeCl_3$, $SnCl_4$, $CuCl_2$, $CrCl_3$, and $AlCl_3$, demonstrate notably higher rates of both cellulose and glucose conversion (>60%) in comparison to Zn^{2+}, Mn^{2+}, and Co^{2+} [10]. The acidity of a reaction can be increased through the formation of a Lewis acid from metal cations like Fe^{3+}, Cr^{3+}, and Al^{3+} when oxidized with water molecules. The presence of halide anions such as I^-, Br^-, and Cl^- to form the Lewis acid/base pair that catalysed the sequential dehydration processes which convert sugars into HMF or furfural [11]. Comparative study by (2014) has found that five promising metal salt acid catalysts, $FeCl_3$, $CuCl_2$, $CrCl_3$, $ZrOCl_2$, and $AlCl_3$, can yield high selectivity of HMF compared to sulphuric acid. $FeCl_3$, in particular, has shown superior performance in terms of HMF production (yielding 42% for corn stover and 41% for maple wood), furfural production (yielding 97% for both maple wood and maize stover), as well as solubilisation of biomass. Boonyakarn *et al.* [12] found that $FeCl_3$ has high acidity (~pH 2.5), which contributes to the catalytic activity for cellulose conversion to glucose. Other metal chlorides with low acidity, such as $MnCl_2$, $CdCl_2$, and $CoCl_2$ (with a pH of around 7), do not exhibit catalytic activity in converting cellulose to glucose. Consequently, the yields of HMF and LA were low. To date, there is no attempt to evaluate nickel (Ni) as a metal catalyst for LA production from cellulose and glucose. Based on the previous studies, Ni has shown potential in promoting the hydrolysis of cellulose by assisting in the destruction of the crystalline cellulose structure, which is an important step in the cellulose hydrolysis reaction [13]. Research by Collard *et al.* [14] also found that Ni assisted in the destruction of the crystalline cellulose structure, which is important in cellulose hydrolysis reactions. While Ni has shown promise in promoting cellulose hydrolysis, particularly by disrupting the crystalline cellulose structure, its catalytic potential in LA synthesis has not been fully studied.

Additionally, this work introduces a novel approach by combining Ni with Fe to synthesize mixed metal catalysts, offering a more efficient and sustainable pathway for cellulose conversion. Both prepared metals are addressed as Fe and Ni only for all catalysts. The combination of these catalysts was addressed as Fe.xNi catalyst, where x refers to the weight %loading of Nickel in the catalyst, for example, Fe.25Ni is 25% nickel and 75% iron in the catalyst. The characteristics of the catalysts are described first, followed by the assessment of the catalytic activity. Commercial cellulose and glucose were used as the raw materials for screening the selected catalysts in terms of LA production.

2. Materials and methods

2.1. Materials

In this study, commercial cellulose and glucose were purchased from Freundemann Schmidt. Other essential materials, including sodium hydroxide, ethanol, acetone, iron (III) chloride, and nickel (II) nitrate, were procured from R&M Chemicals and are of analytical grade. HPLC standards such as glucose, HMF, LA, and formic acid (FA) were bought from Sigma Aldrich.

2.2. Catalyst preparation

Different loadings of iron (III) chloride and nickel (II) nitrate between 25% to 100% were prepared as shown in

10.57647/ijc.2026.1601.02

Table 1. For the Fe. 75Ni catalyst, 6.05 g iron (III) chloride, and 18.58 g nickel (II) nitrate were dissolved in 10 mL of distilled water by stirring at room temperature. A 90 mL mixture of pure ethanol and distilled water (2:1) was added. Then, 10 mL of 6M sodium hydroxide (NaOH) was added as a co-precipitate until the pH reached neutral. To activate the catalyst, the solution was transferred into a Teflon-lined stainless-steel autoclave and subjected to a hydrothermal process at 180 ºC for 12 hours. Subsequently, the solution was cooled to room temperature and a precipitate was obtained after filtration. The powder was then washed repeatedly by using pure ethanol and acetone until the pH of the filtrate was the same as the pH of the wash water. After that, the catalyst produced was oven-dried overnight. Finally, the sample was calcined at 300 °C for three hours to obtain iron-nickel metal catalysts. The resultant materials are designated as Fe.xNi where the $Ni(NO_3)_2$ metal loading was denoted as x as shown in the Table 1 below.

2.3. Catalyst characterization

Fourier Transform Infrared (FTIR) spectroscopy analysis was used to detect and quantify the organic functional groups present in the produced catalysts. The materials underwent analysis using FTIR-ATR (Agilent Technologies) by scanning them in the spectral range of 300–4000 cm^{-1}. X-ray photoelectron spectroscopy (XPS) was used to examine the chemical states of the produced catalysts. The crystalline phase of the catalysts was evaluated using powder X-ray diffraction (XRD) analysis. The study involved scanning instruments within the set range of theta, spanning from 20 to 600, at a 40 min^{-1} scan speed. The porosity of the metal catalysts was analyzed using a nitrogen adsorption/desorption analyzer called the Micromeritics ASAP-2020 instrument (Micromeritics Instrument, Norcross, GA, USA). The Brunauer-Emmett-Teller (BET) and Barret-Joyner-Halenda (BJH) methods were used to identify the pore volume, surface area, and pore size. The acidity of the catalysts was determined using temperature-programmed desorption (TPD) with NH_3 as the probe molecule (TPD-NH_3). The Thermo Finnigan TPD/R/O 1100 equipment, equipped with a thermal conductivity detector (TCD), was employed for this purpose. The catalyst underwent pre-treatment by subjecting it to a flow of N_2 gas for 30 minutes at a temperature of 250 °C. It was then exposed to NH_3 gas for 1 hour at room temperature before being flushed with N_2 gas to eliminate any excess NH_3. The NH_3 desorption peaks were seen in the temperature range of 50 °C to 950 °C using Helium gas flow, which demonstrated the acidity of the catalysts. Field emission scanning electron microscopy (FESEM) model JEOL JSM-7600F was used to analyze the morphology of the catalysts, and this instrument is equipped with an energy dispersive X-ray detector (EDX) (Oxford INCA X-MAC 51 XMX 0021) in order to measure the elemental concentration of the catalyst. An elemental composition and metal loading of the catalysts were determined using an X-ray Fluorescence (XRF) equipment, and this device is integrated with a rhenium anode operating in energy dispersive mode. The stability and thermal analysis were conducted using a thermal analyzer, Mettler Toledo Model: TGA-DSC HT-3, for both thermal gravimetric analysis (TGA) and differential thermal analysis (DTG).

2.4. Catalyst test

The process of hydrolysis to produce LA was carried out in a specialized autoclave reactor. A solution containing 5.0 g of either glucose or cellulose and 0.15 g (3%) of a synthesized catalyst was introduced to the autoclave. The total volume of the solution was 50 mL. Subsequently, the reactor was subjected to a temperature of 180 °C, compressed with nitrogen, and agitated at a speed of 600 rpm for a duration of 5 hours. This technique was continuously observed for catalyst screening as well. After the reaction was completed, the mixture was cooled to room temperature. The reactor employed was a 150 mL stainless steel 316 batch reactor (Model: ACL01-150), renowned for its durability against sulfuric acid. The temperature was controlled using a thermocouple and an electrical heater, while the pressure was maintained by sealing the reactor with six bolts.

2.5. Product analysis

The concentration of the hydrolysis products, such as monosaccharides (glucose) and volatile components (LA, HMF, and FA), was determined using high-performance liquid chromatography (HPLC). The glucose yield (%) based on theoretical yield is calculated using the following formula:

$$Glucose\ Yield\ (\%)\ based\ on\ theoritical\ yield = \frac{Conc\ of\ glucose\ \left(\frac{g}{L}\right) x\ volume\ (L)\ x\ conversion\ fact(1) or}{mass\ of\ cellulose\ (g)} x\ 100 \quad (1)$$

Here, 0.9 is the conversion factor for glucose (which is derived from 162/180). The value 180 represents the molecular weight of glucose, while 162 represents the molecular weight of the monosaccharide units in cellulose. For the yield calculations of LA, HMF, and FA, the following equ. is used:

$$Product\ Yield\ (\%)\ based\ on\ theoritical\ yield = \frac{Conc\ of\ product\ (g/L)\ x\ volume\ (L)}{mass\ of\ cellulose\ (g)\ \ x\ conversion\ factor} x\ 100 \quad (2)$$

10.57647/ijc.2026.1601.02

Table 1. Different loading of $FeCl_3$ and $Ni(NO_3)_2$

Catalyst	Iron (III) chloride, $FeCl_3$	Nickel (II) nitrate, $Ni(NO_3)_2$
Fe.25Ni	75%	25%
Fe.50Ni	50%	50%
Fe.75Ni	25%	75%
Fe	100%	0%
Ni	0%	100%

The conversion factors are specific to each product based on their molecular weight relative to the molecular weight of cellulose: HMF is 0.77 (molecular weight 126), LA is 0.71 (molecular weight 46), while FA is 0.28 (molecular weight 116). To compare the yield of levulinic acid (LA) with previous studies that reported yield in weight percentage, the following calculation is used:

$$LA\ Yield\ (wt\%)\ \frac{Weight\ of\ LA\ (g)}{Weight\ of\ cellulose\ (g)}\ x\ 100 \quad (3)$$

3. Results and discussion

3.1. Structural, phase, and chemical component

The XRD profiles of metal catalysts are shown in Fig. 1. The XRD patterns indicate that elements Fe and Ni in all catalysts are not present in the form of single metal but metal oxide (Fe_2O_3 and NiO). A broad diffraction peak was presented at 2θ (21.7°, 33.185°, 35.585°, 38.98°, 49.485°, 54.085° and 62.485°) which correspond to the diffraction planes (012), (104), (110), (113), (024), (116) and (214), respectively in all catalysts except Ni catalyst. The position and relative strength of diffraction peaks closely match the standard data for hematite, Fe_2O_3 (JCPDS file No. 33-0664), giving further evidence of the high purity of the synthesized Fe_2O_3.

These findings are consistent with the study by Hassan *et al.* [15] and Li *et al.* [16]. XRD result also presents five main peaks at 37.3°, 43.1°, 64.8°, 75.3°, and 79.5° in all catalysts except the Fe catalyst, which correspond to the (111), (200), (220), (311), and (222) planes of NiO (JCPDS NO. 47-1049), respectively. The XRD pattern for NiO is similar to the findings from Fazlali *et al.* [17] and Xu *et al.* [18]. The crystallite size of the catalysts was presented in Table 2, calculated based on the Scherrer equation. Fe.75Ni has a moderate crystallite size of 18.94 nm which is smaller than Fe.50Ni (23.01 nm) but larger than Fe.25Ni (17.32 nm) and Fe (16.88 nm).

This moderate crystallite size likely strikes a balance between having sufficient active sites and maintaining stability under reaction conditions. Smaller crystallite sizes (like in Fe and Ni) typically result in a higher surface area and a greater number of active sites. However, too small crystallite sizes can sometimes lead to less stability and reduced catalytic performance over time.

The larger crystallite size of Fe.50Ni (23.01 nm) may reduce the number of active sites available for the reaction leading to a lower LA yield compared to Fe.75Ni. Fe_2O_3 is a product from the calcination of iron (II) hydroxide ($Fe(OH)_3$) and nickel oxide (NiO) from the calcination of nickel (II) hydroxide (Ni(OH)2), as shown in the following Equs. 4 and 5.

$$2Fe(OH)_3(s) \rightarrow Fe_2O_3(s) + 3H_2O(g) \quad (4)$$

$$Ni(OH)_2(s) \rightarrow NiO(s) + H_2O(g) \quad (5)$$

Meanwhile, $Fe(OH)_3$ is produced from the precipitation of iron (III) chloride ($FeCl_3$) with NaOH as shown in Equ. 6. Similar to $Fe(OH)_2$, $Ni(OH)_2$ is the product from the precipitation of $Ni(NO_3)_2$ with NaOH, expressed in Equ. 7.

$$FeCl_3\ (aq) + 3NaOH\ (aq) \rightarrow Fe(OH)_3(s) + 3NaCl\ (aq) \quad (6)$$

$$Ni(NO_3)_2\ (aq) + 2NaOH\ (aq) \rightarrow Ni(OH)_2(s) + 2NaNO_3\ (aq) \quad (7)$$

The functional groups available on the catalyst were identified using FTIR, and results are displayed in Fig. 2. The peak observed at 455 cm^{-1} is assigned to the stretching and bending vibrations of Fe–O bonds in α-Fe_2O_3 [19]. The intense absorption peaks observed at 526 cm^{-1} are attributed to the vibrational modes of the Fe-O bond [20]. Both of these peaks are present in all metal catalysts except the Ni catalyst, indicating that Fe metal was successfully incorporated and is present in the mixed metal catalysts. The appearance of strong vibrations at 525 cm^{-1} suggests the presence of Ni–O bonds in the fingerprint area [21].

The region at approximately 3340 cm^{-1} is associated with hydroxyl group (OH) activities, which is supported by the study conducted by Salim *et al.* [22]. Based on the research by Saravanakkumar *et al.* [23], the band observed at around 1100 cm^{-1} can be attributed to the stretching mode of the Ni-O-Ni bond. Comparing these results with similar FTIR spectra in the literature, the peaks observed in our catalysts closely align with those found in iron oxide-based materials, such as the typical absorption peaks for Fe–O at 451 and 531 cm^{-1} in Fe_2O_3 [24]. In our study, similar peaks at 455 cm^{-1} and 526 cm^{-1} were observed, suggesting that the Fe–O bonds in our mixed metal catalysts are consistent with those reported for iron oxide phases. In conclusion, the result obtained from the FTIR spectrum proved that the existing functional groups associated with both Ni and Fe in the catalysts produced are consistent with the XRD findings.

10.57647/ijc.2026.1601.02

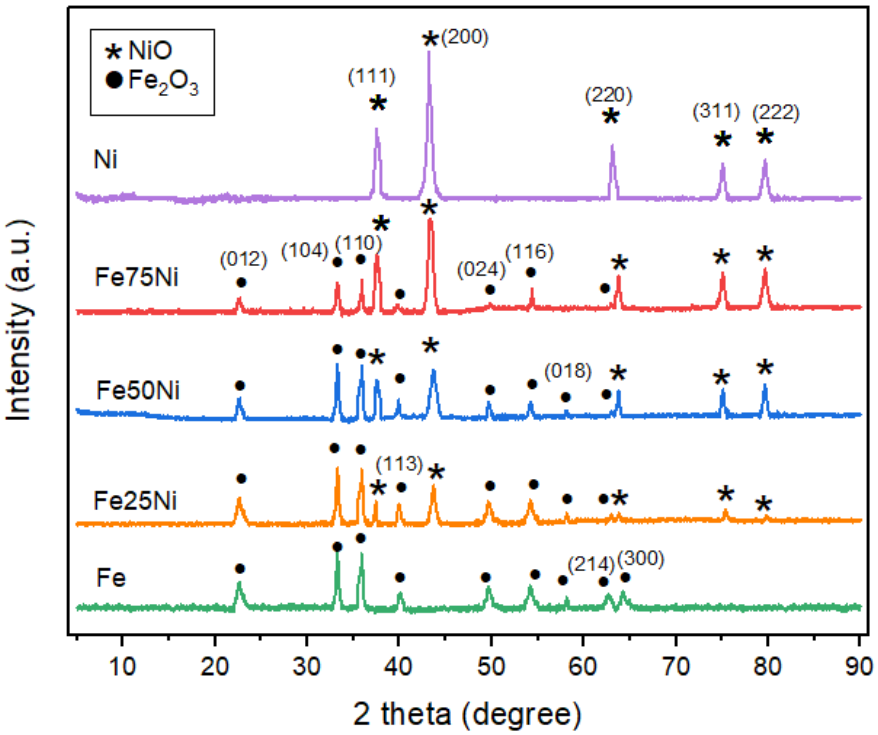

Figure 1. XRD analysis for Fe, Ni and Fe.xNi catalysts

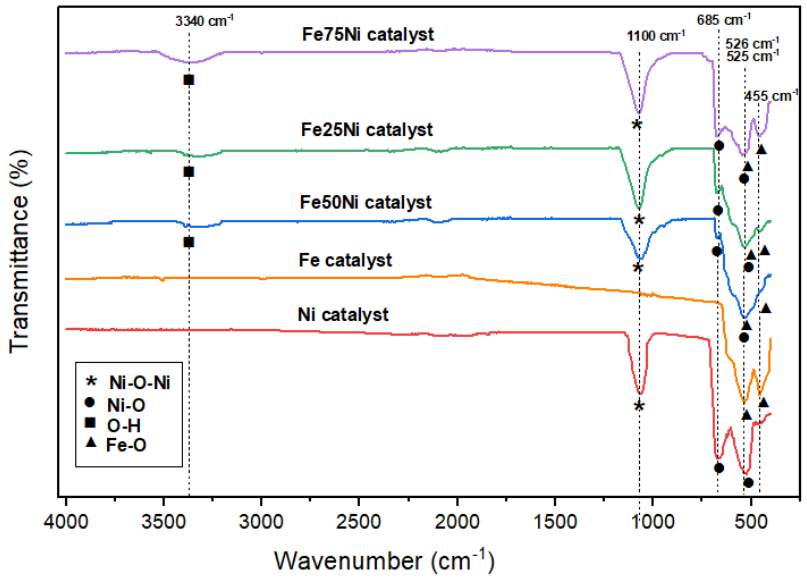

Figure 2. FTIR analysis for Fe, Ni and Fe.xNi catalysts

The TGA and DTG of metal catalysts are shown in Fig. 3 to demonstrate the weight losses of catalysts with increasing temperature. TGA result reveals a first-step weight reduction occurring below 100 °C for all catalysts, which can be attributed to the removal of both physically adsorbed water and the dehydration of surface hydroxyl groups [25]. The second step occurred as a result of the breakdown of hydroxyl metal into metal oxides at temperatures ranging from 200 to 400 ºC. These chemical reactions are similar to the findings by Feyzi and Hassankhani [26] and Pinto *et al.* [27]. These reactions were also confirmed by XRD analysis, as shown in Equ. 4 to 7. Based on Equ. 4, calcination of iron (II) hydroxide ($Fe(OH)_3$) at high temperature produced iron (III) oxide (Fe_2O_3). $Fe(OH)_3$ is a product of the precipitation of iron (III) chloride ($FeCl_3$) with NaOH, as shown in Equ. 6. Meanwhile, calcination of nickel (II) hydroxide ($Ni(OH)_2$) at high temperatures generated nickel oxide (NiO). Similar to $Fe(OH)_2$, $Ni(OH)_2$ is the product formed by precipitation of $Ni(NO_3)_2$ with NaOH, expressed in Equ. 7. Regarding catalytic activity, several key conclusions can be drawn from the TGA curves. The first step of weight loss below 100 °C is indicative of the presence of adsorbed water and hydroxyl groups, which is important for understanding the catalyst's surface chemistry. A stable surface without excessive water or

10.57647/ijc.2026.1601.02

hydroxyl content is desirable for catalytic efficiency, as these species may hinder reactant adsorption and the catalytic process. The second-step weight loss between 200 and 400 °C is linked to the decomposition of hydroxyl metal into metal oxides, which are critical active sites for catalytic reactions. TGA results demonstrate that all prepared Fe.xNi catalysts were stable up to 200 °C, as shown in Fig. 3(c)-(e) and suitable for the production of LA as the reaction was performed within this temperature range. The weight loss observed at higher temperatures is likely due to the decomposition of the metal oxide structures. This is an important consideration when optimizing the operating conditions for catalytic reactions, which could lead to a loss in active sites and catalytic efficiency.

For deeper understanding, the catalyst was analyzed by XPS to identify the surface composition and chemical oxidation states of the surface species in terms of iron, oxygen and nickel. Only one catalyst was selected, Fe.75Ni catalyst because this catalyst produced the highest yield of LA which is discussed in the next section (Section 4.2.5). The wide scan was carried out between 0 and 1200 eV of energy binding as shown in Fig. 4(a). The wide scan provides an overview of the elemental composition present on the catalyst surface.

The XPS spectra in Fig. 4(b) reveal that the catalyst exhibited a Ni $2p_{3/2}$ peak at a binding energy of around 852.25 eV, indicating the presence of Ni^{2+}. Additionally, Ni $2p_{1/2}$ peaks were observed at a binding energy of 870.25 eV, which is attributed to Ni^{3+} [28]. Moreover, the peaks at 858.50 eV and 877.51 eV are ascribed to satellite peaks of the Ni species [29]. The Fe 2*p* core-level XPS spectrum in Fig. 4(c) exhibits two shakeup satellites at 714.9 and 717.7 eV, along with two strong peaks at 722.33 and 710.05 eV.

These peaks correspond to the Fe $2p_{1/2}$ and Fe $2p_{3/2}$ peaks, respectively, which are the characterization of Fe^{3+} and closely match the peaks observed in Fe_2O_3 [30]. The main component of the catalyst namely Fe_2O_3 and NiO in the sample is further confirmed by the O 1*s* signal of the XPS spectrum as illustrated in Fig. 4(d) which can be divided into two peaks.

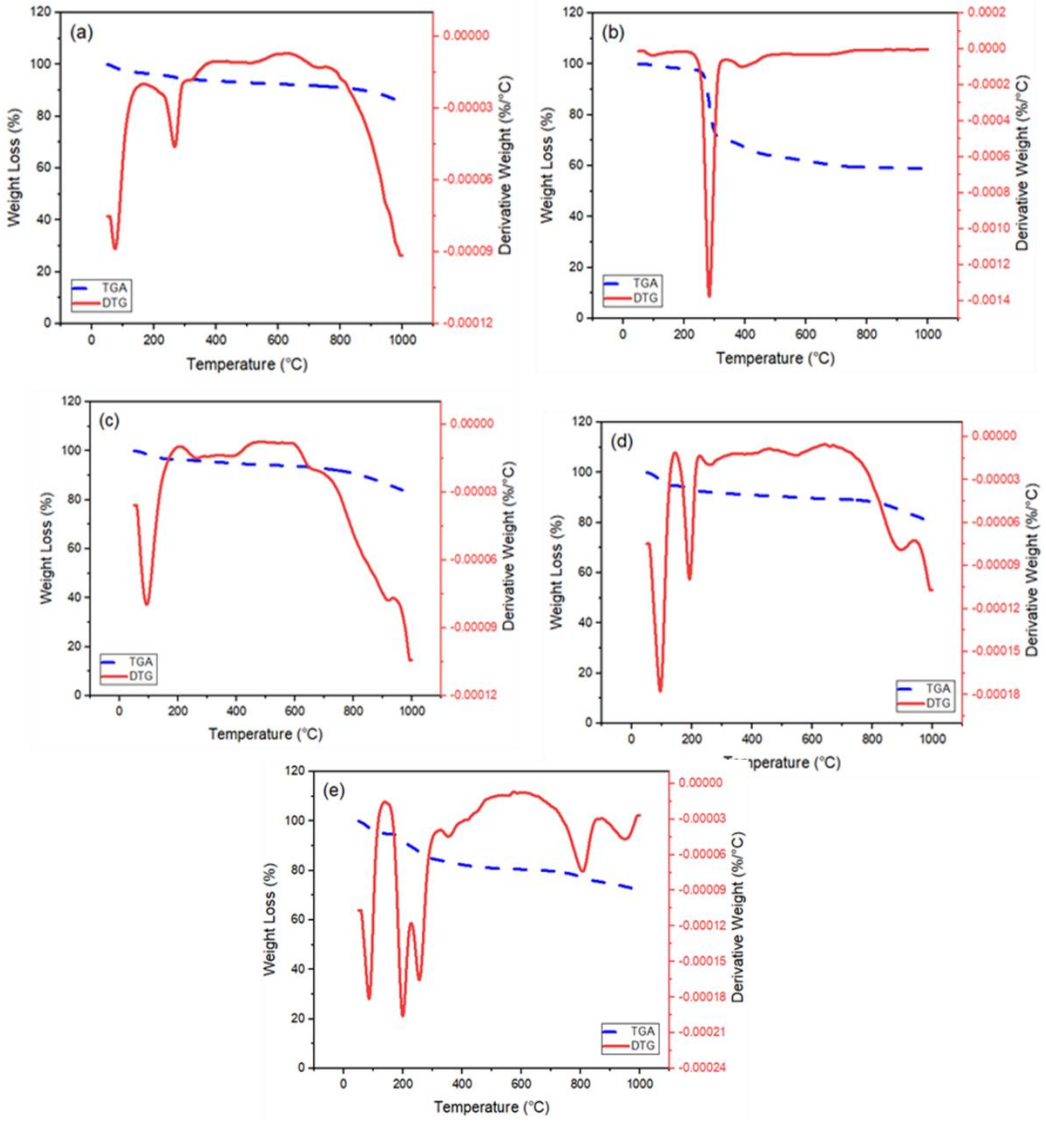

Figure 3. TGA and DTG curves of catalyst (a) Fe, (b) Ni, (c) Fe.25Ni, (d) Fe.50Ni and (e) Fe.75Ni

10.57647/ijc.2026.1601.02

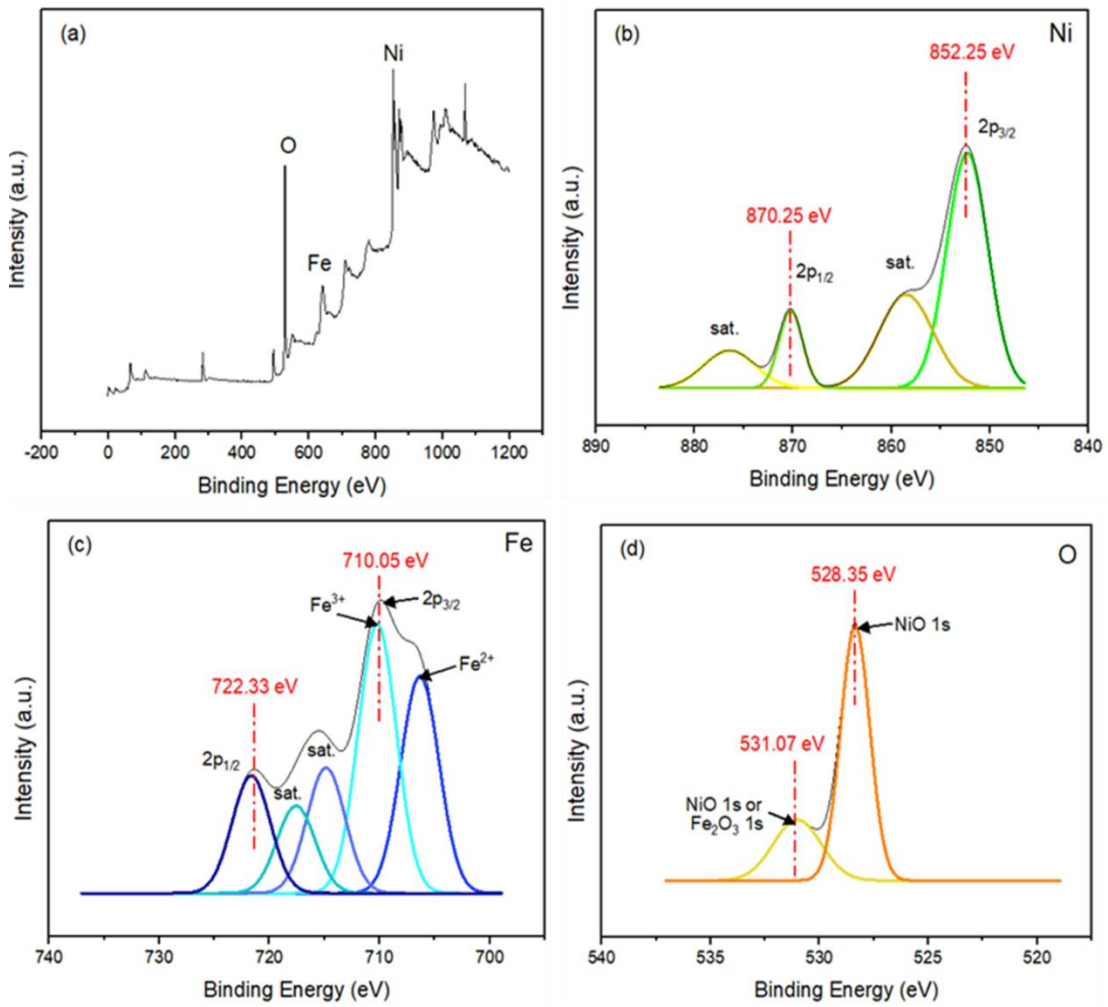

Figure 4. XPS analysis of Fe.75Ni catalyst (a) wide scan (b) Ni 2p (c) Fe 2p and (d) O 1s

The peak located at 528.35 eV corresponds to Ni-O bonds while those located at 531.07 eV refer to Ni-O or Fe-O bonds, similar to the findings by Jiang *et al.* [31] . Consequently, the developed catalyst consisted of NiO and Fe_2O_3 which has already been confirmed via XRD analysis.

3.2. Surface area and porosity

The textural characteristics of all catalysts obtained from N_2 adsorption-desorption isotherms are provided in Table 2. The BET-specific surface areas of Fe.25Ni, Fe.50Ni, Fe.75Ni, Fe and Ni catalysts were found to be 33.09, 15.89, 48.17, 5.63 and 52.96 m^2/g, respectively. The results indicate that the Fe.75Ni and Ni catalysts exhibited higher surface areas compared to the other metal catalysts. The trend of surface area follows Ni > Fe.75Ni > Fe.25Ni > Fe.50Ni > Fe. It is observed that the BET surface area increased as NiO content increased, which is similar to the findings by Hu and Teng [32].

The BET surface area of the Ni catalyst (52.96 m^2/g) is lower than NiO catalyst (188 m^2/g) reported by Tong et al 92015), but higher the NiO catalyst (28.4 m2/g) studied Xu *et al.* [18]. The differences in surface area may be attributed to the various preparation methods and heating techniques used. In case of mixed metal catalysts, the surface areas declined to 15.89 – 48.17 m^2/g with further increase in the Fe content. This could be attributed to the accumulation of Fe_2O_3 crystallites validated in the XRD result which is discussed in a section above (Section 4.2.1). The larger surface area of Fe.75Ni and Ni catalysts can be effectively associated with the significant pore volume (> 0.10 cm^3/g), which is mostly attributed to the increased amount of liquid nitrogen adsorbed [33]. The pore properties of the catalyst, including pore sizes and diameters, are presented in Table 2.

The pore sizes vary from 3.60 to 8.24 nm, indicating that the catalyst is a mesoporous material. According to IUPAC classification, nanoporous materials are categorized into three primary types based on pore size: microporous materials (pore size < 2 nm), mesoporous materials (pore size 2–50 nm), and macroporous materials (pore size > 50 nm) [34]. The Ni and Fe.50Ni catalysts showed similar pore diameters ranging from 8.04 to 8.24 nm. The Fe.50Ni exhibited a high pore diameter, even though the pore volume was low, most likely due to the adsorption of liquid nitrogen occurring on the external surface area rather than filling the micropores [33].

The N_2 adsorption-desorption isotherms are shown in Fig. 5, while the pore size distribution curves are illustrated in Fig. 6. The isotherms for all the catalysts exhibit a type IV profile, which is a characteristic of mesoporousmaterials. The presence of a desorption hysteresis loop (H3 type) confirms the coexistence of mesoporous (2–50 nm) in the catalyst structures [15]. The H3 classification is specific to solid materials composed of flexible, non-rigid aggregates or agglomerates of plate-like particles, resulting in extensive non-uniform slit-shaped pores [15]. The pore size distribution curve in Fig. 6 shows that the average pore sizes of all metal catalysts are within the range of 2–18 nm. For Ni, Fe.50Ni and Fe.75Ni catalysts, the pore size distribution gave a climbing peak observed at the high-pressure region, indicating the presence of prominent mesoporous characteristics in these catalysts [35]. The likewise trend for pore size distribution of Fe in Fig. 6(a) and Fe.25Ni in Fig. 6(d) are observed due to the blockage of pore when the amount of Fe was high.

3.3. Acid sites properties

The acidity characteristics of the catalysts, as determined by the amount of ammonia uptake, are presented in Table 3. The acidity data ranks Ni > Fe.75Ni > Fe.50Ni > Fe.25Ni > Fe. Based on the XRD analysis, the Fe catalyst is referred to as Fe_2O_3, while the Ni catalyst is referred to as NiO. Therefore, the comparison of acidity with previous studies was done by comparing the total acidity of Fe_2O_3 and NiO. The results indicate that the Fe catalyst possesses slightly weak acidic site properties, while the Ni catalyst showed the highest weak acid sites with total acidity (15.57 mmol/g). This is higher than the total acidity for Fe_2O_3 in other studies, which ranged from 1.75 to 2.60 mmol/g (Atius and Astuli, 2021 and Preda *et al.* [36]. In comparison to other studies, the total acidity observed for NiO is significantly higher, reflecting its more prominent role in catalysis due to a greater concentration of weak acid sites.The inclusion of NiO species in the catalytic system enhances the presence of acidic sites, as confirmed by Hafriz *et al.* [37]. The acidity strength is determined by the quantity of adsorbed NH_3 at various desorption temperatures, where weak acidity refers to desorption temperatures below 573 K, medium-strong acidity refers to desorption temperatures ranging from 573 K to 773 K, and strong acidity corresponds to desorption temperatures above 773 K [38]. The ammonia desorption profiles of metal catalysts, shown in Fig. 7, reveal the presence of weak, medium, and strong acid sites. The Fe.75Ni catalyst exhibits a broader and more pronounced NH_3 desorption peaks across the temperature range of 473-1273 K, indicating aa higher concentration of acid sites compared to other mixed metal Fe.xNi catalysts. This broad desorption peak range suggests the existence of both Brønsted and Lewis acid sites, which are crucial for various catalytic reactions. The profile for Ni catalyst shows the highest peak of weak acids, suggesting that the catalyst is rich with weak acids from Lewis acid species. The inclusion of both iron and nickel in the catalyst promotes the development of Lewis acid sites [39].

Table 2. Physical properties of Fe.xNi catalysts

Catalyst	[a]BET Surface Area (m^2/g)	[a]Pore Volume (cm^3/g)	[a]Pore Size/ Diameter (nm)	Crystallite size (nm)[b]
Fe.25Ni	33.09	0.0340	3.60	17.3171
Fe.50Ni	15.89	0.0478	8.24	23.0146
Fe.75Ni	48.17	0.1141	6.44	18.9391
Fe	5.63	0.0110	4.63	16.8759
Ni	52.96	0.1677	8.04	16.1925

a) Determined by using BET analysis.
b) Calculated using Scherer Equation determined from XRD data.

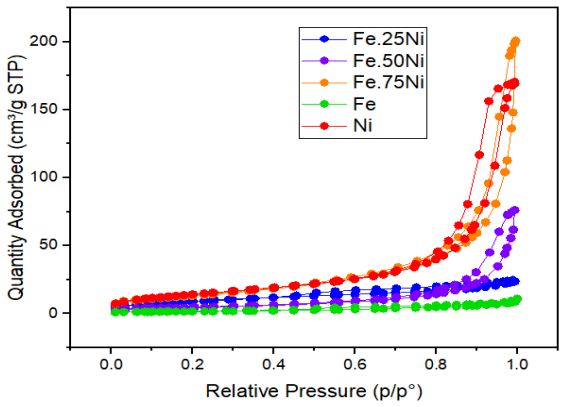

Figure 5. Isotherm profiles of Fe, Ni and Fe.xNi catalysts

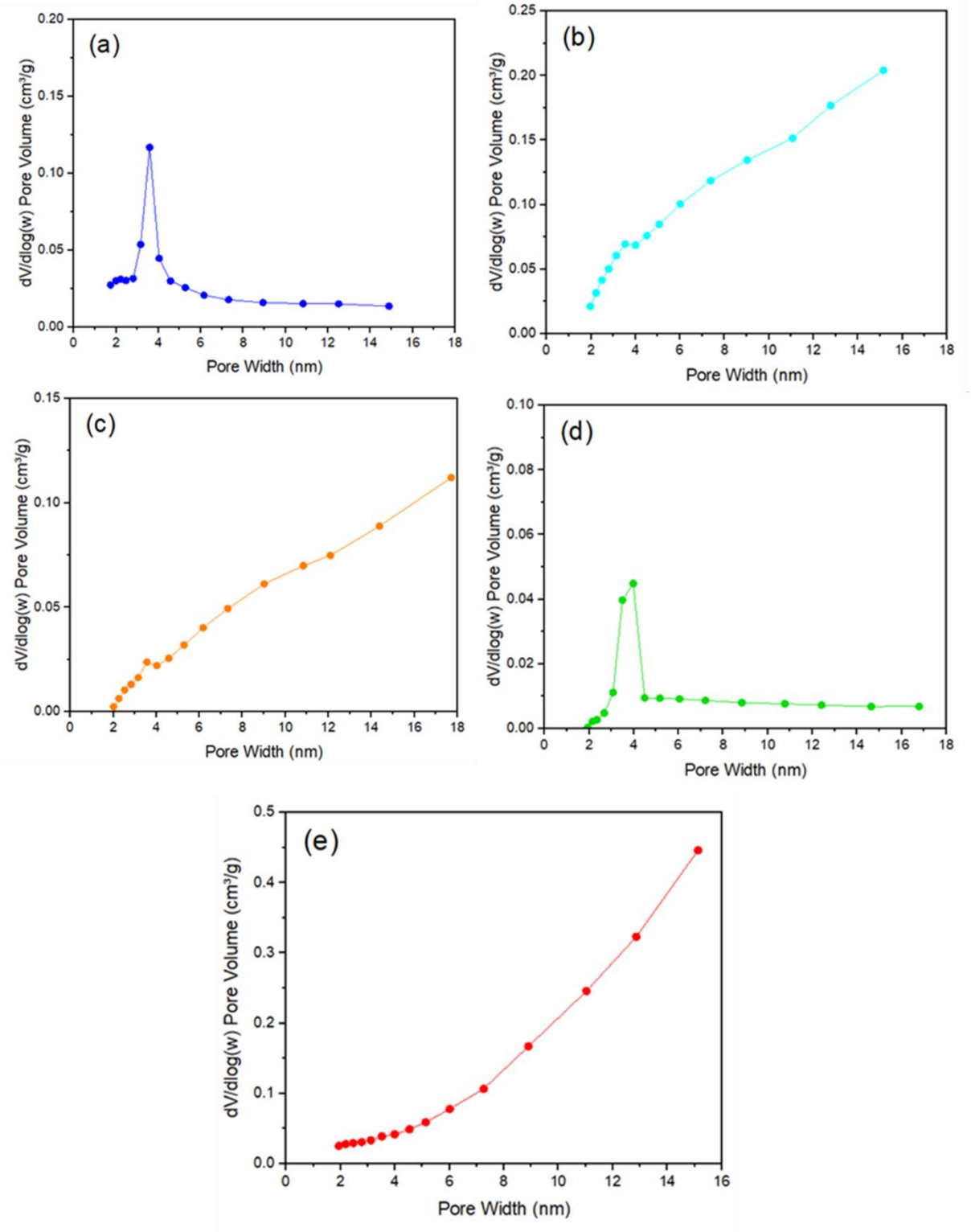

Figure 6. Distribution of pore volume of (a) Fe.25Ni (b) Fe.50Ni (c) Fe.75Ni (d) Fe and (e) Ni catalysts

Table 3. Acidity data of Fe.xNi catalysts

Catalyst	Total amount NH_3 adsorbed[a] (mmol/g)
Fe.25Ni	3.26
Fe.50Ni	4.96
Fe.75Ni	8.39
Fe	1.44
Ni	15.57

a)NH_3-TPD desorption peak for all catalysts

10.57647/ijc.2026.1601.02

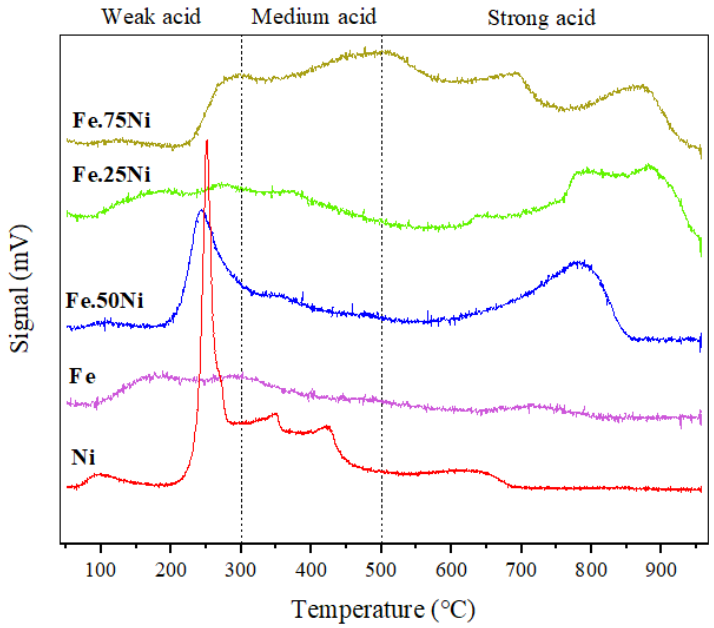

Figure 7. NH_3-TPD patterns of Fe and Ni catalysts

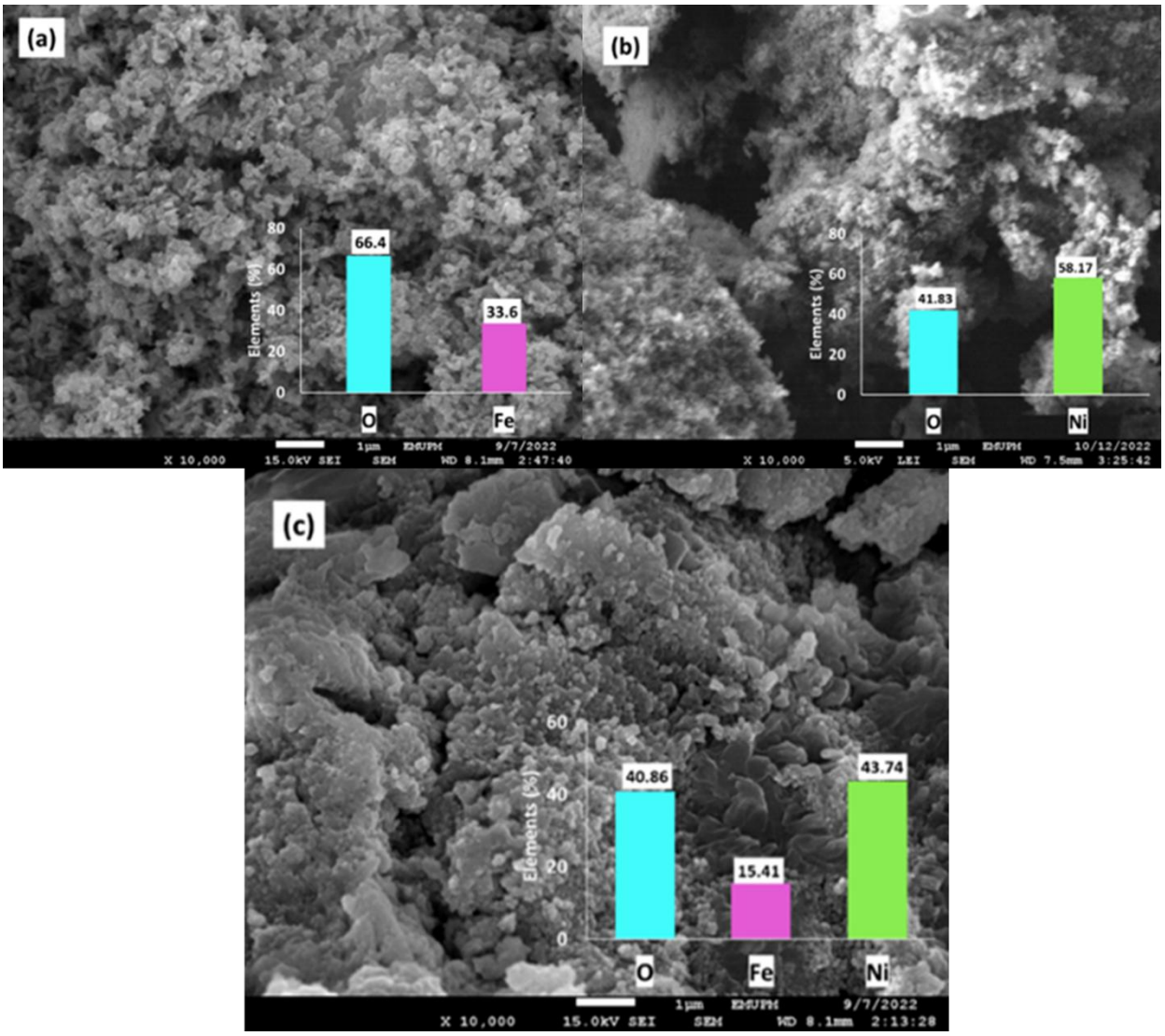

Figure 8. FESEM images and EDX analysis for (a) Fe catalyst (b) Ni catalyst and (c) Fe.75Ni catalyst

10.57647/ijc.2026.1601.02

After the incorporation of Ni with Fe, the peaks for medium and strong acids were increased, which made the catalysts highly active with both weak and strong acid sites of Lewis acid species. In comparison with other catalysts, the enhanced desorption at medium to high temperatures further suggests the increased strength of the acid sites as a result of the incorporation of Ni into the Fe catalyst. This enhanced acidity is likely a contributing factor to the improved catalytic performance of the Fe.75Ni catalyst. In this hydrolysis process, hydroxide (OH) ligands are formed, which act as electron pair donors. The OH ligands that are generated increase the acidity of the metal cations and thus improve their ability to donate electrons [9].

3.4. Surface morphology

The surface morphology of the catalysts was examined using FESEM images, which were captured at 10,000x as shown in Fig. 8. The particles for both Fe and Ni catalysts appear to be spherical in shape and exhibit some degree of agglomeration. This agglomeration may be due to the magnetic character of the particles, whereby they attract and come into close proximity with one another [40]. The particles also exhibit non-uniformity, which can be attributed to particle agglomeration [41].

Interestingly, insignificant changes were observed between single metal (Fe or Ni) and the Fe.75Ni catalyst, suggesting that the combination of iron and nickel in the Fe.75Ni catalyst does not significantly alter the morphology structure of the catalyst. These features may enhance the active and accessible surface area for the reaction [42]. The FESEM images also depict the presence of string-like structures on the spherical particles. These features may enhance the active and accessible surface area for the reaction, potentially contributing to the catalytic efficiency. The elemental composition of the catalyst was analyzed using EDX spectroscopy, and the results are reported as a bar chart in Fig. 8. The EDX analysis of the Fe. 75Ni catalyst confirms the successful incorporation of NiO and Fe_2O_3 metal oxides. However, the results show that the actual Ni content was only 40%, instead of the expected 75%, while the Fe content was 10% instead of the intended 25%.

This deviation may be due to the presence of oxygen in the formation of NiO or Fe_2O_3. To further validate the metal composition, X-ray fluorescence (XRF) analysis was performed, and the results are presented in Table 4. The XRF data provide the amount of Fe and Ni without the influence of oxygen, and the minor variations in the composition are within an acceptable range. It can be concluded that the precipitation method is a practical and efficient method for introducing metal catalysts.

In addition to EDX analysis, the elemental distribution mapping of the Fe.75Ni catalyst was performed to provide a detailed understanding of the spatial distribution on these elements on the catalyst surface. The mapping images, shown in Fig. 9, reveal the distribution of iron, nickel, and oxygen, which can be referred to as NiO and Fe_2O_3 metal oxides.

The uniform distribution is crucial for the catalytic activity, as it ensures that the active sites are evenly distributed, allowing efficient reaction kinetics and improved catalytic performance.

3.5. Conversion of cellulose and glucose into LA

The catalytic activity of Fe and Ni-based catalysts was evaluated for the production of LA and other intermediate products using two different raw materials: cellulose and glucose. The performance of catalyst, including Fe, Ni, Fe.25Ni, Fe.50Ni and Fe.75Ni, was compared, as shown in Fig. 10(a) and 10(b) for cellulose and glucose, respectively. The catalytic activity was assessed at a temperature of 180 ºC and a reaction time of 5 hours.

For the synthesis of LA from cellulose, the highest yield of LA (10.51 %) based on theoretical yield was obtained from Fe.75Ni catalyst and the yield based on weight percentage was 7.52 wt.%. This catalyst outperforms others, including Ni (with a 6.37% yield) and Fe (with only 2.92% yield), which can be attributed to the unique synergy between Fe and Ni species.

The Fe.75Ni catalyst's increased yield correlates with its enhanced surface area and acidity as detailed in the BET and NH_3-TPD results which indicate a higher number of available acid sites. The trend of LA production from cellulose was Fe.75Ni > Ni > Fe.50Ni > Fe.25Ni > Fe.

Table 4. Elemental composition of Fe.xNi catalysts determined by XRF

Catalysts	XRF analysis (wt.%)			Actual composition value (wt.%)	
	Fe	Ni	Others	Fe	Ni
Fe	98.2	-	1.9	100.0	-
Ni	-	99.8	0.2	-	100.0
Fe.25Ni	73.2	24.5	2.3	75.0	25.0
Fe.50Ni	51.9	47.4	0.8	50.0	50.0
Fe.75Ni	22.4	77.1	0.46	25.0	75.0

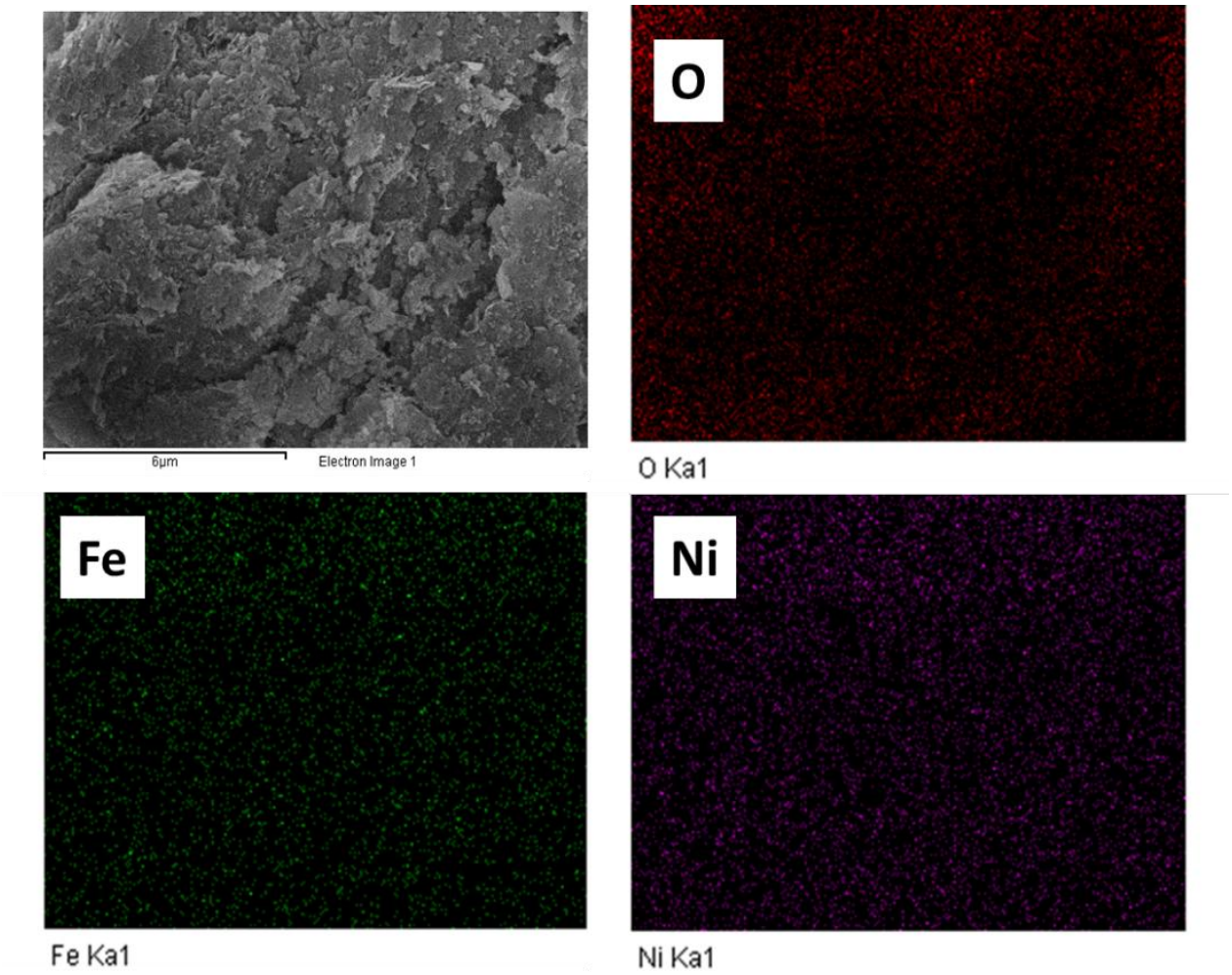

Figure 9. EDX mapping for Fe.75Ni

When using glucose as the raw material, the highest yield of LA (32.32 %) of theoretical was achieved also from the Fe.75Ni catalyst, with the yield based on weight percentage at 20.82 wt.%. Notably, the highest surface area was observed in the Ni catalyst (52.96 m^2/g), which corresponds to its excellent catalytic activity in glucose conversion, yielding 16.93% of LA.

However, the Fe.75Ni catalyst, which had a slightly lower surface area (48.17 m^2/g), achieved a higher LA yield, suggesting that surface area alone may not fully explain the catalytic behavior. The synergy between Fe and Ni in Fe . 75Ni, which provides a combination of stronger Lewis acid sites and efficient porosity, is likely the key factor that enhances the catalytic efficiency as discussed further in the NH_3-TPD and pore size distribution sections. To confirm the role of the catalyst, a blank sample was conducted without Fe.xNi catalyst. The yields of HMF and LA from glucose were 0.04% and 7.33% of theoretical, respectively. For cellulose, the yields of HMF and LA were 0.11% and 0.92% of the theoretical values, respectively.

The significant difference in the yields between the samples with and without Fe.xNi catalyst confirmed the crucial role of these catalysts in the biomass conversion reactions. The function of Fe in our catalytic system is mainly associated with its strong Lewis acidity.

Fe^{3+} ions quickly undergo hydrolysis in aqueous environments, producing highly reactive Lewis acid sites crucial for facilitating the dehydration and rehydration processes of cellulose-derived intermediates into levulinic acid [10]. Conversely, Ni primarily provides weaker Lewis acid sites and facilitates the degradation of crystalline cellulose, thus enhancing the accessibility of cellulose chains for hydrolysis [13]. When utilized individually, Fe demonstrated lower LA yields compared to Ni, as it was incapable of effectively disrupting the crystalline structure of cellulose. When Fe was coupled with Ni, the catalytic activity was markedly enhanced due to the dual advantages of robust Lewis acidity from Fe and cellulose structural disruption facilitated by Ni. The synergy was obviously evident in the Fe.75Ni catalyst, which demonstrated the maximum yield of LA. The result of LA in this study is also higher than the result obtained in a study by Boonyakarn et al. [12] using the combination of Brønsted hydrothermal carbon-based and Lewis acid catalysts to produce LA from cellulose. This indicates that the application of Lewis acid alone is sufficient to produce a high yield of LA.

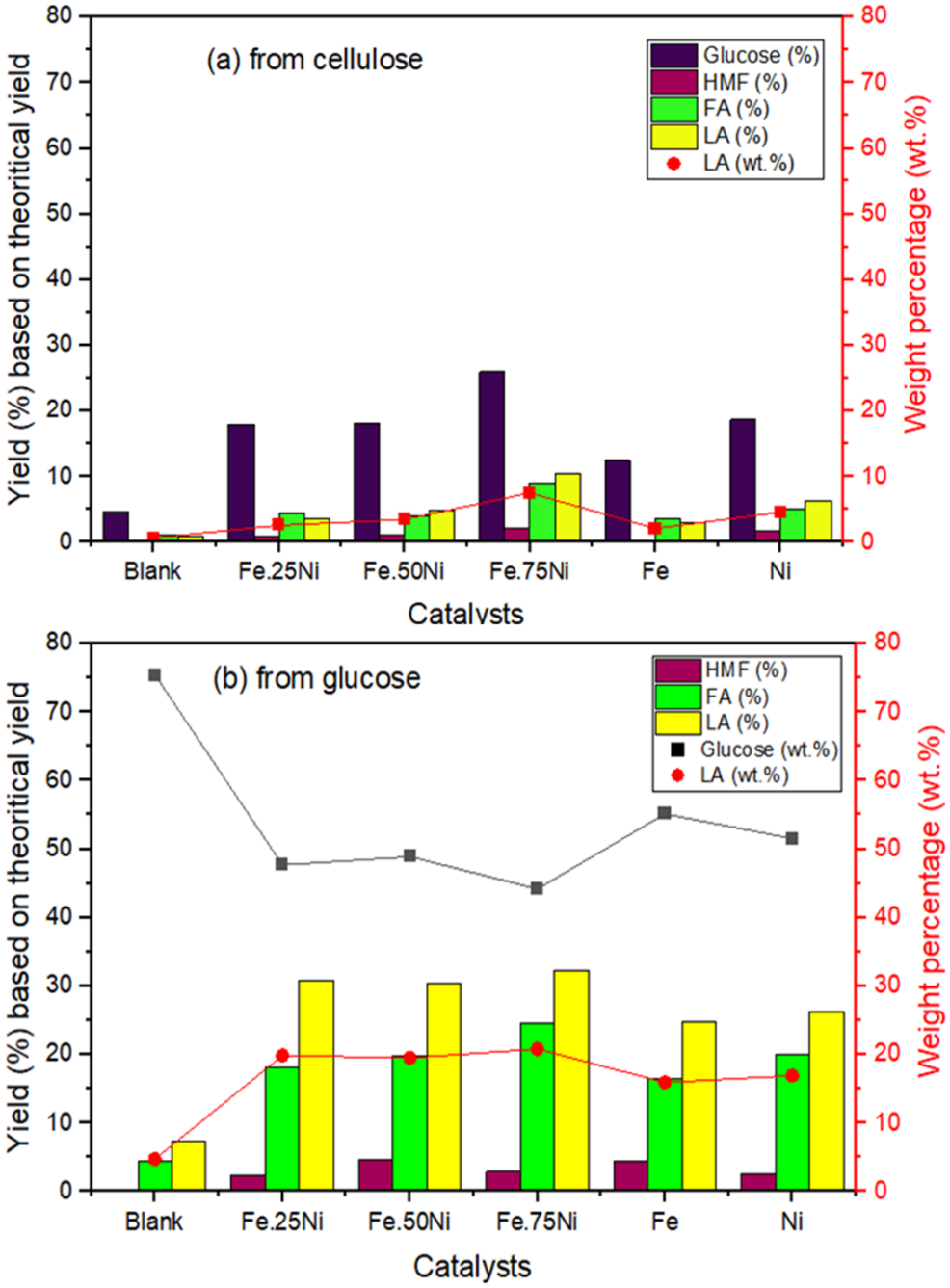

Figure 10. Product yields (%) based on theoretical yield and LA yield (wt%) from cellulose (a) and glucose (b) using Fe.xNi catalysts. Reaction conditions: 5 g cellulose or glucose, reaction temperature 180 ºC, reaction time 5 h, catalyst dosage 0.15 g

The results from the experiments using both cellulose and glucose as raw material indicate that Fe.75Ni is the best performance in terms of LA production. The physicochemical characteristics of the catalysts, such as their porosity and acidity, are related to the distribution of the products from the reactions [43]. The Fe.75Ni catalyst has a high acidity value and a large number of acid sites, as confirmed by the TPD-NH_3 analysis. The chemical route of converting cellulose or glucose to LA requires a high concentration of acid sites [44]. While the Ni catalyst had the highest acidity value, the type of acidity also influenced LA production [45]. The combination of Fe and Ni in the Fe.75Ni catalysts produced highly strong LewisLewis's acid, whereas the Ni catalyst can only generate weak Lewis acid sites. The pore size of the catalyst also influenced the yield of LA from cellulose or glucose. Furthermore, the size of mesopores among the metal catalysts (3.60-8.24 nm) was smaller compared to the cellulose molecule (40–300 μm) [46] but larger than the glucose molecule (0.54 to 0.97 nm) [47]. Therefore, during the cellulose conversion process, the reaction could only take place outside the Fe-Ni catalysts because cellulose was unable to pass through the catalysts' pores. After cellulose was transformed into glucose, the molecules may enter the catalysts.

In addition to the observed trends in LA production, it is important to note that the lower LA yields from the catalyst with greater Fe loading can be assumed due to the

production of an additional by-product, such as lactic acid (Ramli and Amin [48]. The amount of FA was lower than the LA yield for all the reactions. This could be due to the breakdown of FA under the reaction conditions. A study by Ya'Aini *et al.* [49] found that FA has been seen to undergo breakdown into carbon monoxide (CO), carbon dioxide (CO_2), water (H_2O), and hydrogen gas (H_2) under conditions of heat and acidity. As shown in Fig. 10, the presence of glucose and HMF as intermediates in the final products suggests that the conversion process was not fully optimized. Furthermore, a study by Wang et al. [50] produces the highest amount of LA when conducted experiment at 240 °C for 6 hours using metal oxide catalyst. This indicates that further optimization of reaction conditions or modifications to the catalysts may be necessary to enhance the conversion and selectivity towards the desired LA product. Based on various analyses and reaction results, a mechanism for the conversion of cellulose to LA catalyzed by Fe.xNi catalyst was proposed, as illustrated in Fig. 11. It can be observed that the products mainly contained glucose, HMF, and LA. Fe^{2+} and Fe^{3+} (from Fe_2O_3) and Ni^{+} act as Lewis acids, promoting bond cleavage of cellulose and promoting the glucose isomerization into fructose [51].

3.5.1. *Optimization of conditions*

The production of LA from glucose was examined under different experimental conditions, including reaction temperature, catalyst loading, and reaction time. These parameters significantly impacted the yield of LA and provided insights into optimizing the reaction conditions for efficient production. Glucose was selected as the feedstock due to its high conversion efficiency, availability, and ability to dissolve in the reaction solvent. Meanwhile, for the catalyst, Fe.75Ni was used based on the highest result from the catalyst screening. Temperature plays a pivotal role in the hydrolysis and subsequent conversion of glucose into LA, significantly influencing the reaction and the formation of both desired and undesired products.

As demonstrated in Fig. 12, increasing the reaction temperature from 120°C to 200°C resulted in a substantial increase in LA yield with a rise from 16.74% at 120°C to 34.92% at 200°C. The increased temperature helps to break the glycosidic bonds of glucose more efficiently and leads to the formation of HMF as a key intermediate in the conversion of sugars to LA [52]. At temperatures of 160°C and above, the reaction favors the conversion of glucose to HMF, followed by rapid conversion of HMF to LA, which confirms the expected reaction pathways. This is consistent with findings from similar studies where the formation of LA was observed to increase with temperature concurrently with the increasing of HMF formation.

However, it is important to note that while temperature is a crucial factor for enhancing LA yield beyond 200°C, the formation of by-products like humin was possible to rise significantly [53].

These side reactions potentially hinder the optimal production of LA, leading to a decrease in overall process efficiency. The concentration of HMF, an important intermediate, still remained relatively high at 200°C, although the LA yield reached 34.92%, which suggests that the conversion of glucose into HMF still happened. However, it was not possible to reach temperatures above 200 °C because of reactor constraints.

Catalyst loading is a crucial parameter that significantly impacts the efficiency of LA production in glucose conversion reactions.

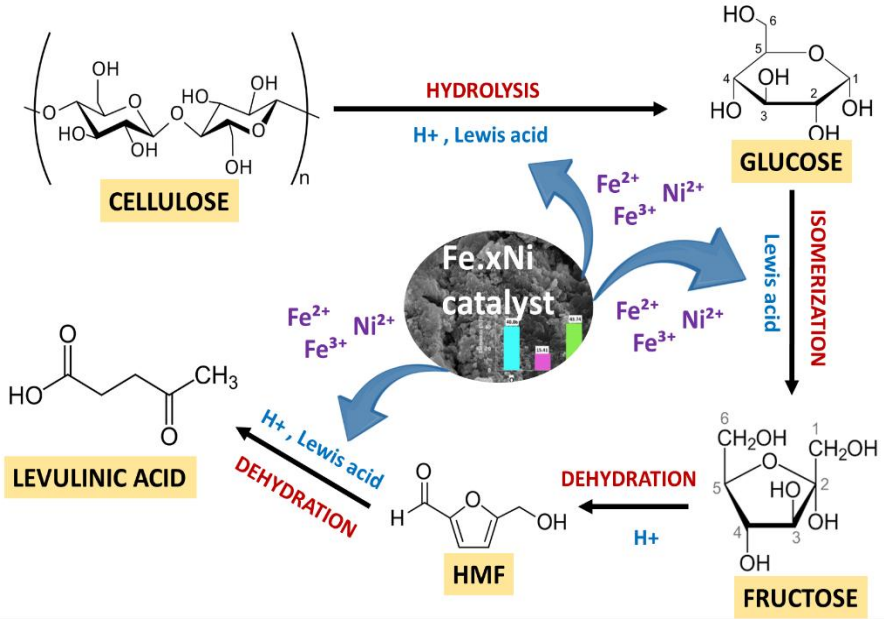

Figure 11. Schematic diagram of the catalytic conversion process of cellulose to LA over the Fe.xNi catalyst

10.57647/ijc.2026.1601.02

As presented in Fig. 13, increasing the catalyst loading from 0.05 g to 0.4 g resulted in an initial increase in LA yield, with the highest LA wt% of 29.72% observed at a catalyst loading of 0.3 g. This trend suggests that as catalyst loading increases, more active sites are available for the reaction, thereby enhancing the rate of glucose conversion to LA.

A higher catalyst loading typically improves the efficiency of the reaction by facilitating the breakdown of glucose and promoting the formation of intermediates, such as those that are crucial for LA production. This aligns with findings from other studies where an increase in catalyst loading has been associated with enhanced catalytic activity due to a greater number of available sites for adsorption and reaction.

However, the data also reveals a slight decrease in LA yield when the catalyst loading is further increased to 0.4 g, with the LA wt% dropping to 25.08%. This reduction in LA yield at higher catalyst loadings highlights a critical aspect of catalyst behaviour. Excessive catalyst loading can lead to several issues that negatively impact the efficiency of the reaction.

First, an overabundance of catalyst may introduce side reactions that result in the formation of unwanted by-products. It was expected that the higher catalyst loading may have promoted the formation of humins or other side products, which can block the active sites or interfere with the catalytic process, thereby reducing the overall yield of LA.Reaction time also significantly impacts the yield of LA.

The results in Fig. 14 demonstrate that as the reaction time increased from 3 hours to 9 hours, the LA yield initially increased and reached 46.18% at 5 hours. However, further extension of the reaction time led to a gradual decline in LA yield from 29.72% at 5 hours to 26.18% at 9 hours.

This decrease can be attributed to the formation of humins and other polymeric by-products, which not only reduce the concentration of the desired product but also contribute to catalyst deactivation.

These findings suggest that longer reaction times can enhance the yield up to an optimal point, but excessive reaction time leads to the formation of undesirable by-products that decrease overall LA production.

3.5.2. *Reusability of catalyst*

The reusability and stability of catalysts are fundamental factors that influence the long-term viability of catalytic processes, particularly in industrial applications where catalyst replacement is costly.

In this study, the performance of an Fe.75Ni catalyst was assessed over five consecutive reaction cycles to evaluate its ability to retain activity and generate LA efficiently, as shown in Fig. 15.

The experimental setup was optimized to operate at a reaction temperature of 200°C for a period of 5 hours using glucose as the feedstock and a catalyst loading of 0.3 g. Initial results revealed that the LA yield from the fresh catalyst was 46.18% (29.72 mass%), indicating efficient glucose and HMF conversion.

However, as the catalyst underwent repeated cycles, a marked decline in catalytic performance was observed. By the fourth cycle, the LA yield had decreased to 24.49% (15.72 mass%) and further reduced to 11.47% (8.65 mass%) in the fifth cycle. This trend suggests a progressive loss of catalytic efficiency, which is typically associated with catalyst deactivation.

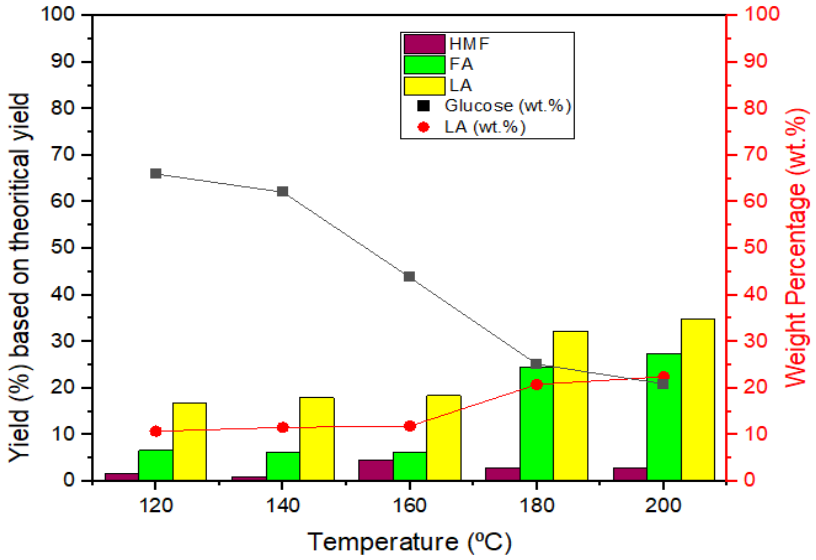

Figure 12. Product yields (%) based on theoretical yield and LA yield (wt%) from glucose at different temperatures using Fe.75Ni catalysts. Reaction conditions: 5 g glucose, 5 h and catalyst dosage 0.15 g

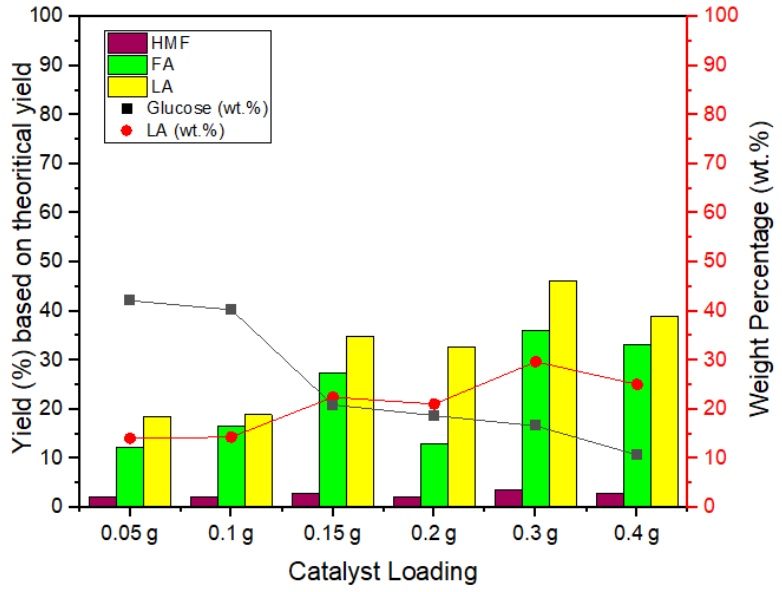

Figure 13. Product yields (%) based on theoretical yield and LA yield (wt%) from glucose using different loadings of Fe.75Ni catalysts. Reaction conditions: 5 g glucose, 200 ºC and reaction time 5 h

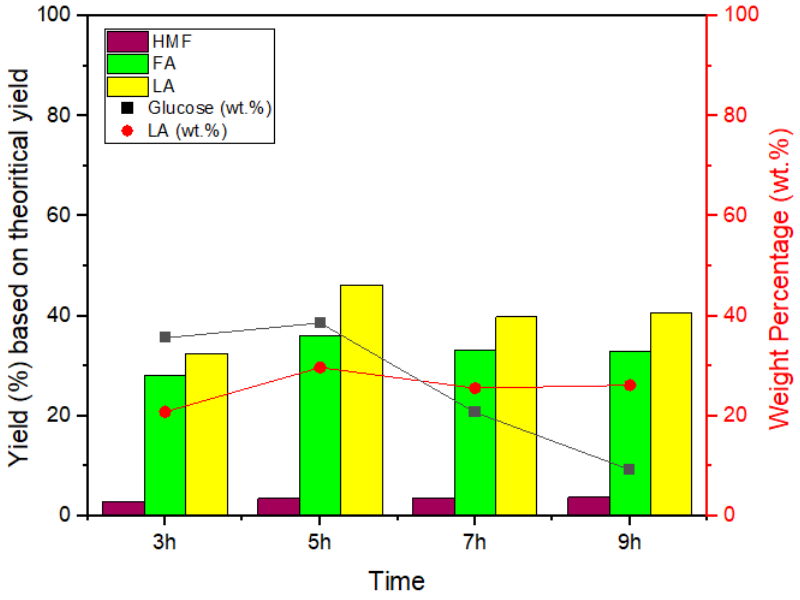

Figure 14. Product yields (%) based on theoretical yield and LA yield (wt%) from glucose at different times using Fe.75Ni catalysts. Reaction conditions: 5 g glucose, 200 ºC and catalyst dosage 0.30 g

The underlying cause of this decline can be attributed to the loss of active sites, which are essential for facilitating the desired reactions. To gain a deeper understanding of the catalyst's deactivation, the NH_3 absorption capacity of both the fresh and spent catalysts was measured using TPD-NH_3 analysis.

The fresh catalyst demonstrated an NH_3 absorption rate of 8.39 mmol/g, indicating a high availability of acid sites. In contrast, the spent catalyst exhibited a significantly reduced NH_3 absorption capacity of only 0.38 mmol/g. This reduction in acid site concentration correlates with the observed decrease in LA yield, supporting the hypothesis that the loss of acidic active sites is directly responsible for the catalyst's diminished performance [53]. The catalyst deactivation observed in this study is consistent with previous research in the field, which has shown that the reusability of catalysts is influenced by the amount of acid sites [43].

The cleaning procedure, involving hexane and methanol washes to remove polar and non-polar impurities, may also contribute to the leaching of these acid sites, thereby accelerating catalyst deactivation [54]. The findings of this study, which show a substantial reduction in LA yield and NH_3 absorption after multiple cycles, further highlight the need for methods to restore catalyst activity after each reuse.

10.57647/ijc.2026.1601.02

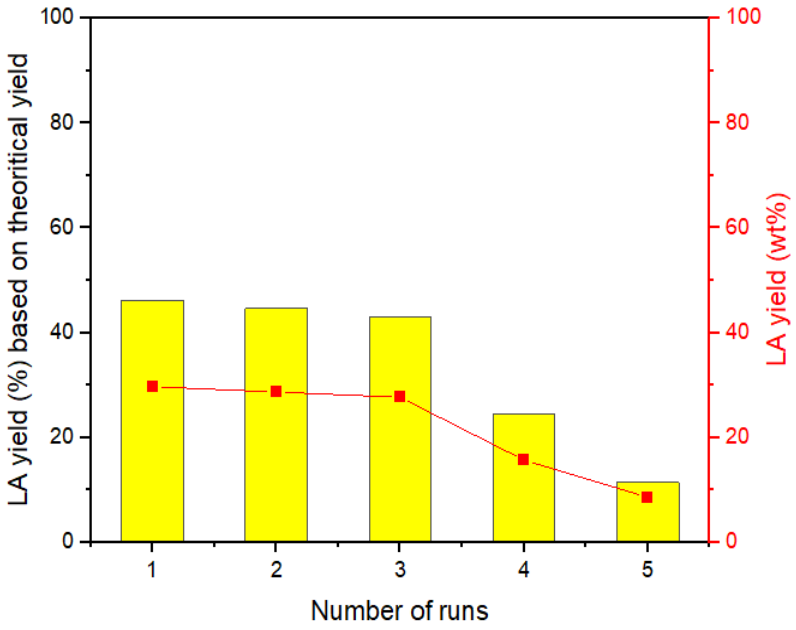

Figure 15. Reusability study of Fe.75Ni catalyst. Reaction conditions: 5g glucose, reaction temperature 200 ºC, reaction time 5h and catalyst dosage 0.30 g

4. Conclusion

In conclusion, the catalytic performance of various Fe and Ni loadings was evaluated, revealing that the Fe.75Ni catalyst demonstrated the highest activity among the synthesized catalysts (Fe, Ni, Fe.25Ni, Fe.50Ni).

The Fe.75Ni catalyst achieved a maximum LA yield of 32.32% based on theoretical yield or 20.82 wt.% based on weight percentage compared to other catalysts. This performance was observed at a reaction temperature of 180 ºC for a reaction time of 5 hours by using a catalyst loading of 0.15g. The findings suggest that LA production over mixed metal catalysts is predominantly influenced by the catalyst's acidity, while the good surface area also plays a crucial role by providing abundant catalytic sites. The excellent performance of Fe.75Ni is attributed to its high acidity and large acid sites, as well as its appropriate pore size distribution, which facilitate the effective conversion of cellulose and glucose to LA.

The optimal conditions for obtaining the highest LA yield from glucose were identified as a reaction temperature of 200 °C, 0.30 g of Fe.75Ni catalyst, and a reaction duration of 5 hours. Under these conditions, the LA yield reached 46.18% based on the theoretical yield or a weight percentage of 29.72 wt.%. While the Fe.75Ni catalyst demonstrated an initial high activity, but its performance significantly decreased after several cycles due to the loss of acid sites. The reduction in NH_3 absorption and acid site concentration provides strong evidence that the catalyst deactivation is primarily caused by the leaching of these active components.

The study highlights the importance of optimizing both the physical and chemical properties of catalysts to achieve high yields of LA.

While this study focuses on optimizing catalytic performance, the practical application of LA production requires further work, particularly in product purification and isolation. These aspects will be addressed in future research. The results emphasize the potential of mixed metal oxide catalysts, particularly the Fe.75Ni catalyst, in the production of LA from cellulose or glucose and provide a foundation for further research and optimization in this field.

Credit authorship contribution statement

Z.N. Akhlisah: Conceptualization, Methodology, Investigation, Writing - Original Draft W.A.K.G Wan Azlina: Conceptualization, Writing - Review & Editing, Supervision R. Yunus: Conceptualization, Resources, Writing - Review & Editing, Supervision Y.H. Taufiq-Yap: Resources, Supervision U. Rashid: Resources, Supervision G. Abdulkareem-Alsultan: Conceptualization, Methodology N. Asikin-Mijan: Conceptualization, Methodology, Writing - Review & Editing

Declaration of competing interest

The authors declare that they have no known competing financial interests or personal relationships that could have appeared to influence the work reported in this paper.

Acknowledgments

The authors would like to express their appreciation for the scholarship under the German Academic Exchange Service (DAAD) and the Southeast Asian Regional Center for Graduate Study and Research in Agriculture (SEARCA).

References

[1] Y. Shen, Y. Xu, J. Sun, B. Wang, F. Xu, R. Sun, Catal. Commun. **50** (2014) 17–20. https://doi.org/10.1016/j.catcom.2014.02.019

[2] M. Gozan, J.R.H. Panjaitan, D. Tristantini, R. Alamsyah, Y.J. Yoo, Int. J. Chem. Eng. (2018) 1920180. https://doi.org/10.1155/2018/1920180

[3] K. Lappalainen, Y. Dong, Biomass and Bioenergy **123** (2019) 159–165. https://doi.org/10.1016/j.biombioe.2019.02.017

[4] Z.N. Akhlisah, W.A.K.G. Wan Azlina, R. Yunus, Y.H. Taufiq-Yap, U. Rashid, Malaysian J. Sci. Adv. Technol. **4** (2024) 374–382. http://doi.org/10.56532/mjsat.v4i3.348

[5] W. Zhao, Y. Li, C. Song, S. Liu, X. Li, J. Long, Appl. Energy **204** (2017) 1094–1100. https://doi.org/10.1016/j.apenergy.2017.03.116

[6] X. Zhang, X. Zhang, N. Sun, S. Wang, X. Wang, Z. Jiang, Renew. Energy 141 (2019) 802–813. https://doi.org/10.1016/j.renene.2019.04.058

[7] P. Joolaei, S. Farshineh, G.A. El-hiti, K. Kumar, J. Cho, S. Rezania, Chem. Eng. Res. Des. **201** (2024) 176–184. https://doi.org/10.1016/j.cherd.2023.11.059

[8] L. Peng, A. Bahadoran, S. Sheidaei, P. Joolaei, Renew. Energy **224** (2024) 120050. https://doi.org/10.1016/j.renene.2024.120050

[9] C.M. Cai, N. Nagane, R. Kumar, C.E. Wyman, Green Chem. **16** (2014) 3819–3829. https://doi.org/10.1039/C4GC00747F

[10] N.S.M. Azlan, C.L. Yap, S. Gan, M.B.A. Rahman, Ind. Crops Prod. **181** (2022) 114778. https://doi.org/10.1016/j.indcrop.2022.114778

[11] G. Marcotullio, W. De Jong, Green Chem. **12** (2010) 1739–1746. https://doi.org/10.1039/b927424c

[12] T. Boonyakarn, P. Wataniyakul, P. Boonnoun, A.T. Quitain, T. Kida, M. Sasaki, N. Laosiripojana, B. Jongsomjit, A. Shotipruk, Ind. Eng. Chem. Res. **58** (2019) 2697–2703. https://doi.org/10.1021/acs.iecr.8b05332

[13] S. Zhang, F. Jin, J. Hu, Z. Huo, Bioresour. Technol. **102** (2011) 1998–2003. https://doi.org/10.1016/j.biortech.2010.09.049

[14] F.X. Collard, A. Bensakhria, M. Drobek, G. Volle, J. Blin, Biomass and Bioenergy **80** (2015) 52–62. https://doi.org/10.1016/j.biombioe.2015.04.032

[15] N. Hassan, A. Shahat, A. El-Didamony, M.G. El-Desouky, A.A. El-Bindary, J. Mol. Struct. **1217** (2020) 128361. https://doi.org/10.1016/j.molstruc.2020.128361

[16] X. Li, H. Yu, X. Xue, Procedia Environ. Sci. **31** (2016) 582–588. https://doi.org/10.1016/j.proenv.2016.02.092

[17] F. Fazlali, A. Mahjoub, R. Abazari, Solid State Sci. **48** (2019) 263–269. https://doi.org/10.1016/j.solidstatesciences.2015.08.022

[18] M. xin Xu, H.X. Wang, H. dong Ouyang, L. Zhao, Q. Lu, J. Hazard. Mater. **401** (2021) 123334. https://doi.org/10.1016/j.jhazmat.2020.123334

[19] M. Dutt, K. Suhasini, A. Ratan, J. Shah, R.K.K. Vaishali, J. Mater. Sci. Mater. Electron. **0** (2018) 0. https://doi.org/10.1007/s10854-018-0186-7

[20] W.J. Aziz, M.A. Abid, D.A. Kadhim, M.K. Mejbel, IOP Conf. Ser. Mater. Sci. Eng. **881** (2020) 012099. https://doi.org/10.1088/1757-899X/881/1/012099

[21] J. Moavi, F. Buazar, M.H. Sayahi, Sci. Rep. (2021) 1–14. https://doi.org/10.1038/s41598-021-85832-z

[22] R. Salim, J. Asik, M. Sani, Wood Sci. Technol. **55** (2021) 295–313. https://doi.org/10.1007/s00226-020-01258-2

[23] D. Saravanakkumar, R. Karthika, S. Ganasaravanan, S. Sivaranjani, S. Pandiarajan, B. Ravikumar, A. Ayeshamariam, J. Appl. Physic. **10** (2018) 73–83. https://doi.org/10.9790/4861-1003027383

[24] A. Norouzi, A. Nezamzadeh-Ejhieh, Phys. B Phys. Condens. Matter **599** (2020) 412422 Contents. https://doi.org/10.1016/j.physb.2020.412422

[25] M.A. Abdullah, M.S. Nazir, M.R. Raza, B.A. Wahjoedi, A.W. Yussof, J. Clean. Prod. **126** (2016) 686–697. https://doi.org/10.1016/j.jclepro.2016.03.107

[26] M. Feyzi, A. Hassankhani, J. Nat. Gas Chem. **20** (2011) 677–686. https://doi.org/10.1016/S1003-9953(10)60241-1

[27] P.S. Pinto, G.D. Lanza, J.D. Ardisson, R.M. Lago, J. Braz. Chem. Soc. **30** (2019) 310–317. https://doi.org/10.21577/0103-5053.20180179

[28] L. Chu, S. Gu, Q. Jin, P. Zhu, Y. Shen, P. Li, Int. J. Hydrogen Energy **45** (2020) 28752–28763. https://doi.org/10.1016/j.ijhydene.2020.07.223

[29] A.G. Ramu, M.L.A. Kumari, M.S. Elshikh, H.H. Alkhamis, A.F. Alrefaei, D. Choi, Chemosphere **271** (2021) 129475. https://doi.org/10.1016/j.chemosphere.2020.129475

[30] Y. Zhang, Q. Wang, K. Zhu, K. Ye, G. Wang, D. Cao, J. Yan, Chem. Eng. J. **428** (2022). https://doi.org/10.1016/j.cej.2021.131204

[31] L. Jiang, J. Wang, X. Wu, G. Zhang, Water. Air. Soil Pollut. **228** (2017). https://doi.org/10.1007/s11270-017-3646-4

[32] C.C. Hu, H. Teng, J. Catal. **272** (2010) 1–8. https://doi.org/10.1016/j.jcat.2010.03.020

[33] N. Azri, R. Irmawati, U.I. Nda-Umar, M.I. Saiman, Y.H. Taufiq-Yap, J. King Saud Univ. - Sci. **33** (2021) 101417. https://doi.org/10.1016/j.jksus.2021.101417

[34] S. Kamari, F. Ghorbani, Biomass Convers. Biorefinery **11** (2021) 3001–3009. https://doi.org/10.1007/s13399-020-00637-w

[35] R. Ramachandran, C. Zhao, M. Rajkumar, K. Rajavel, P. Zhu, W. Xuan, Z.X. Xu, F. Wang, Electrochim. Acta **322** (2019) 134771. https://doi.org/10.1016/j.electacta.2019.134771

[36] S. Preda, P. Umek, M. Zaharescu, C. Anastasescu, S. V. Petrescu, C. Gîfu, I. Balint, Catalysts **12** (2022) 666. https://doi.org/10.3390/catal12060666

[37] R.S.R.M. Hafriz, N.A. Arifin, A. Salmiaton, R. Yunus, Y.H. Taufiq-yap, Fuel **308** (2022) 122041. https://doi.org/10.1016/j.fuel.2021.122041

[38] H. Huang, J. Liu, X. Liu, J. Xiao, S. Zhong, X. She, Z. Fu, D. Yin, Fuel **182** (2016) 373–381. https://doi.org/10.1016/j.fuel.2016.05.120

[39] M.M. Zainol, W.A. Nazreen, P.I.P. Ylang, T.T. Hoe, M.A.M. Yussuf, N.A.S. Amin, Chem. Eng. Trans. **78** (2020) 547–552. https://doi.org/10.3303/CET2078092

[40] S.M. Rahimi, F.S. Arghavan, A. Othmani, N. Nasseh, Int. J. Environ. Anal. Chem. **00** (2020) 1–21. https://doi.org/10.1080/03067319.2020.1817420

[41] B. Gnana, S. Raj, B. Natesan, A.M. Asiri, J.J. Wu, S. Anandan, Ionics, **26** (2019) 953-960. https://doi.org/10.1007/s11581-019-03236-6

[42] A.R. Yazdanbakhsh, H. Daraei, M. Rafiee, H. Kamali, Water Sci. Technol. **73** (2018) 2998–3007. https://doi.org/10.2166/wst.2016.157

[43] R. Ringgani, M.M. Azis, Rochmadi, A. Budiman, Appl. Biochem. Biotechnol. **194** (2022) 2684–2699. https://doi.org/10.1007/s12010-022-03806-x

[44] W. Weiqi, W. Shubin, Chem. Eng. J. **307** (2017) 389–398. https://doi.org/10.1016/j.cej.2016.08.099

[45] M.A.A. Zarin, M.M. Zainol, N.A.S. Ramli, N.A.S. Amin, Mol. Catal. **528** (2022) 112506. https://doi.org/10.1016/j.mcat.2022.112506

[46] L.K. Kian, N. Saba, M. Jawaid, H. Fouad, Int. J. Biol. Macromol. **156** (2020) 347–353. https://doi.org/10.1016/j.ijbiomac.2020.04.015

[47] L. Yang, B. Zhang, Y. Liang, B. Yang, T. Kong, L.M. Zhang, Carbohydr. Res. **343** (2008) 2463–2467. https://doi.org/10.1016/j.carres.2008.06.031

[48] N.A.S. Ramli, N.A.S. Amin, Appl. Catal. B Environ. **163** (2015) 487–498. https://doi.org/10.1016/j.apcatb.2014.08.031

[49] N. Ya'Aini, N.A.S. Amin, S. Endud, Microporous Mesoporous Mater. **171** (2013) 14–23. https://doi.org/10.1016/j.micromeso.2013.01.002

[50] K. Wang, Y. Liu, W. Wu, Y. Chen, L. Fang, W. Li, H. Ji, Catal. Letters **150** (2020) 322–331. https://doi.org/10.1007/s10562-019-03023-y

[51] X. Xu, B. Liang, Y. Zhu, J. Chen, T. Gan, H. Hu, Y. Zhang, Z. Huang, Y. Qin, Bioresour. Technol. **387** (2023) 129600. https://doi.org/10.1016/j.biortech.2023.129600

[52] L. Chuaboon, C. Saengsen, O. Sookbampen, E. Yang, H. Shukor, Y. Chisti, W. Rongwong, Waste and Biomass Valorization (2024). https://doi.org/10.1007/s12649-024-02500-9

[53] C.E. Bounoukta, C. Megías-Sayago, S. Ivanova, F. Ammari, M.A. Centeno, J.A. Odriozola, Fuel **318** (2022) 123712. https://doi.org/10.1016/j.fuel.2022.123712

[54] H. Mavakumba, R. Yunus, U. Rashid, Y.H. Taufiq-yap, J. Environ. Chem. Eng. **7** (2019) 102993. https://doi.org/10.1016/j.jece.2019.102993